

0017-9310(94)00221-5

A model of inverse segregation: the role of microporosity

V. R. VOLLER and SURESH SUNDARRAJ

Department of Civil Engineering, 500 Pillsbury Drive, University of Minnesota, Minneapolis, MN 55455, U.S.A.

(Received 11 October 1993 and in final form 13 July 1994)

Abstract—A numerical model of inverse segregation in a vertically cast unidirectionally solidified aluminum–copper binary alloy is presented. The model predicts the solute concentration distribution up the length of the casting. The model is validated on comparison with available analytical solutions. Initial comparisons with experiments show that the model predicts a non-physical region of positive segregation in the upper part of the casting. On accounting for microporosity formation, however, the model predictions show close agreement with experimental measurements. Application of the model also demonstrates the need to correctly account for microsegregation processes.

INTRODUCTION

Recently, there has been much activity in the modeling of macrosegregation [1–4] (the redistribution of solute phases during the solidification of an initially uniform melt of a multicomponent alloy). A commonly studied macrosegregation system is the solidification of a binary material [1–3], initially at a uniform concentration, against a vertical isothermal wall. In this system, as the solidification proceeds, the solute is rejected and subsequently redistributed by solutal and thermally driven natural convection flows. An alternative macrosegregation system results from the unidirectional solidification of a binary alloy, e.g. aluminum–copper, cooled from below. If the solute phase is heavier than the solvent and the partition coefficient $k_0 < 1$, then the system will be both thermally and solutally stable. During this solidification, the shrinkage that occurs as the solid + liquid mushy region forms establishes a flow of the inter-dendritic fluid towards the chill face. This flow redistributes the rejected solute phase and forms macrosegregation known as ‘inverse segregation’ [5–11]. A typical concentration profile on complete solidification, shown in Fig. 1, is a positively segregated region in the vicinity of the chill, a ‘steady-state’ region in the mid-section of the ingot, and a negatively segregated region near the top of the ingot.

The objective of the current paper is the development of an inverse segregation model, in an aluminum–copper system, based on the fundamental heat and solutal transport equations. This work is related to the macrosegregation study reported by Diao and Tsai [12], who used two-dimensional transport equations to describe inverse segregation during the initial stages of solidification. In the current study we include a number of additional and important features in the modeling. In particular:

- (1) the extent of the simulation is carried out to the completion of solidification;
- (2) a full accounting of the density variations within the solid and liquid phases is used [13];
- (3) a treatment of the eutectic reaction [14], where the density change is greatest, is included;
- (4) the effects of microporosity formation on the concentration distribution in the finally solidified casting are studied; and
- (5) a non-equilibrium treatment is invoked that allows for zero mass diffusion in the solid at the local scale (i.e. at the local scale a Scheil assumption is used, as opposed to an equilibrium lever rule assumption).

INVERSE SEGREGATION

Consider a dilute aluminum–copper alloy (a binary eutectic alloy), initially in the molten state, at the nominal concentration C_0 , contained in the insulated mold defined by $0 < x < X_b$ (see Fig. 1). At time $t = 0$, the temperature at the bottom face $x = 0$, is lowered and fixed at a temperature $T_0 < T_{eut}$ (T_{eut} the eutectic

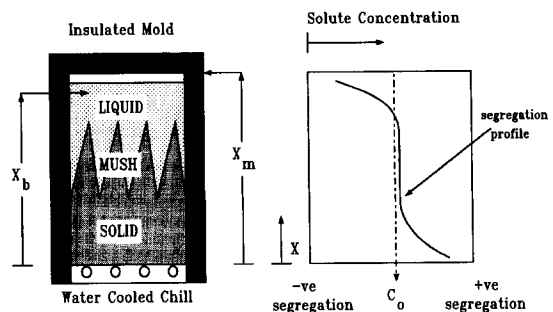


Fig. 1. Inverse segregation: a schematic of unidirectional solidification; a typical concentration profile after complete solidification.

NOMENCLATURE

c_p	specific heat [$J kg^{-1} K^{-1}$]	u_l	liquid velocity in the casting direction [$m s^{-1}$]
C	concentration [mass%]	x	coordinate in domain [m]
$[C]$	mixture concentration [mass%]	X_b	length of the solution domain [m]
C_{eut}	eutectic concentration [mass%]	X_{eut}	position of the eutectic front [m]
C_0	nominal concentration of the alloy [mass%]	X_m	height of the mold [m]
D	mass diffusion coefficient [$m^2 s^{-1}$]	X_{tip}	position of the dendrite tips [m].
ff	friction factor		
F	mass flow rate of liquid per unit area [$kg s^{-1} m^{-2}$]	Greek symbols	
g	volume fraction	ρ	mass density of the alloy
g_{por}	volume fraction of porosity	$[\rho]$	mixture density of the alloy
h_{amb}	heat transfer coefficient [$J m^{-2} s^{-1} K^{-1}$]	$[\rho C]$	mixture solute density
k_0	partition coefficient	$[\rho H]$	mixture enthalpy.
K	thermal conductivity [$J m^{-1} s^{-1} K^{-1}$]	Subscripts	
L	enthalpy of fusion [$J kg^{-1}$]	Al	aluminum
m_1	representative liquidus slope [$K (mass\%)^{-1}$]	b	boundary of the solution domain
S	source term	Cu	copper
t	time [s]	eut	eutectic
Δt	time step [s]	por	porosity
T	temperature [K]	P, W, E	position of the node point
T_{amb}	ambient temperature of the surroundings [K]	l	liquid
T_{eut}	eutectic temperature [K]	tip	dendrite tip
T_f	fusion temperature [K]	s	solid
T_i	initial temperature [K]	w, e	west and east control volume interfaces.
u	system velocity in the casting direction [$m s^{-1}$]	Superscripts	
		o	old value
		*	value at solid-liquid interface.

temperature) such that solidification proceeds unidirectionally from bottom to top. At an instant in time, in this process, three transient regions can be identified: solid, solid+liquid (mushy zone), and liquid. During the solidification, solute is rejected in the mushy region and can be subsequently redistributed by fluid flow. Since, the current system is both thermally and solutally stable, this fluid flow is driven by solidification shrinkage alone. The solute redistributed in this manner results in solute-rich and solute-poor regions in the finally solidified casting, a phenomenon referred to as inverse segregation [10].

Assumptions

A comprehensive analysis of the inverse segregation system requires coupled solution of heat and mass transfer equations describing the transport of heat and solute. In developing appropriate transport equations and an associated numerical model, the following basic assumptions will be used:

(1) the domain is one-dimensional, defined by $0 < x < X_b$, where X_b is the length of the (macro-porosity free) domain on complete solidification;

(2) mass transport in the solid phase by diffusion is neglected; this is typically three or more orders of magnitude smaller than the mass diffusion in the liquid;

(3) the solid phase is stationary;

(4) in the phase diagram the liquids slope m_1 and the partition coefficient k_0 are assumed to be constants;

(5) equilibrium conditions exist at the solid-liquid interface, i.e.

$$T = T_f - m_1 C_l \quad (1)$$

and

$$C_s^* = k_0 C_l \quad (2)$$

where T is the temperature, C is the concentration, T_f is the fusion temperature of pure aluminum, C_s^* is the interface solid concentration and the subscripts s and l stand for solid and liquid phases, respectively;

(6) the specific heats, c_p , and c_{p_l} , and thermal conductivities, K_s and K_l , are constant within each phase, but discontinuous between the solid and liquid; further, the latent heat of fusion L and the liquid mass

diffusivity D_1 are fixed constants and are not functions of temperature and concentration;

(7) due to the relatively rapid nature of heat and liquid mass diffusion, in a microscopic representative elemental averaging volume (REV) [15], the temperature T , the liquid concentration C_1 , the liquid density ρ_1 and the liquid velocity u_1 are assumed to be constant.

Governing equations

The governing equations are derived from the general two-phase volume averaged equations for describing transport phenomena during solidification, presented by Ni and Beckermann [15]. In the current approach appropriate forms of the two-phase equations are additively combined together resulting in the following governing equations:

Energy

$$\frac{\partial[\rho H]}{\partial t} + \nabla \cdot (\rho_1 u c_{p_1} T) + \nabla \cdot (\rho_1 u L) = \nabla \cdot ([K] \nabla T) \quad (3)$$

Species

$$\frac{\partial[\rho C]}{\partial t} + \nabla \cdot (\rho_1 u C_1) = \nabla \cdot (\rho_1 g_1 D_1 \nabla C_1) \quad (4)$$

Mass

$$\frac{\partial[\rho]}{\partial t} + \nabla \cdot (\rho_1 u) = 0. \quad (5)$$

In the above equations, the mixture density is

$$[\rho] = \int_0^{g_s} \rho_s d\alpha + g_1 \rho_1 \quad (6)$$

the mixture enthalpy

$$[\rho H] = c_{p_s} T \int_0^{g_s} \rho_s d\alpha + g_1 \rho_1 c_{p_1} T + g_1 \rho_1 L \quad (7)$$

the mixture solute density

$$[\rho C] = \int_0^{g_s} \rho_s C_s d\alpha + g_1 \rho_1 C_1 \quad (8)$$

the mixture thermal conductivity

$$[K] = g_s K_s + g_1 K_1 \quad (9)$$

and the 'system velocity'

$$u = g_1 u_1. \quad (10)$$

In addition, the temperature scale has been translated so that the eutectic temperature $T_{eut} = 0$. The proposed equations are valid throughout the solidification. In the fully solid region the system velocity $u = 0$ and the inverse segregation problem will reduce to that of diffusion controlled heat transfer.

Treatment of the local scale

The above governing equations are macroscopic equations valid at the scale of the process. Micro-scale

effects are included, however, via the definition of the mixture terms in the REV. In writing down the definitions in equations (6)–(8), the so-called Scheil assumption is invoked, i.e., at the local scale of the REV, mass diffusion is complete in the liquid, but zero in the solid. An alternative local-scale assumption is the equilibrium lever assumption (complete mass diffusion throughout the REV). With such an assumption equations (6)–(8) become

$$[\rho] = g_s \rho_s + g_1 \rho_1 \quad (11)$$

$$[\rho H] = g_s \rho_s c_{p_s} T + g_1 \rho_1 c_{p_1} T + g_1 \rho_1 L \quad (12)$$

and

$$[\rho C] = g_s \rho_s C_s + g_1 \rho_1 C_1. \quad (13)$$

Boundary conditions

The boundary conditions are:

at $x = 0$,

$$u = 0 \quad [K] \frac{\partial T}{\partial x} = h_{amb} (T_{amb} - T|_{x=0}) \quad \frac{\partial C_1}{\partial x} = 0 \quad (14)$$

where h_{amb} is the heat transfer coefficient and T_{amb} is the ambient temperature of the chill;

at $x = X_b$,

$$F_b = \rho_1 u_b \quad \frac{\partial T}{\partial x} = 0 \quad \frac{\partial C_1}{\partial x} = 0. \quad (15)$$

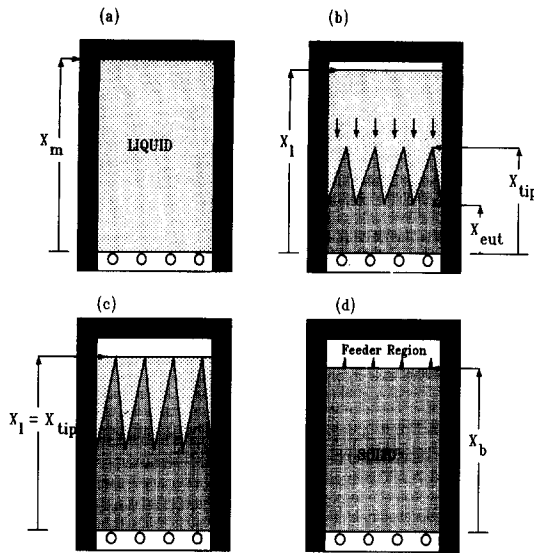
The value F_b is the mass flow rate of liquid per unit area that enters the system to compensate for the shrinkage in $0 < x < X_b$. Note that this mass flux will result in a convective heat flux and solutal mass flux at $x = X_b$ of the form

$$q_h = F_b (c_{p_1} T|_{x=X_b} + L) \quad (16)$$

and

$$q_c = F_b C_1|_{x=X_b}. \quad (17)$$

Correct application of these boundary conditions requires careful definition of the point $x = X_b$. Initially, before solidification commences, the liquid metal occupies a region $0 < x < X_m$, where X_m is the height of the mold cavity [Fig. 2(a)]. When solidification starts, the level of the liquid metal drops to feed the shrinkage, forming an air-liquid interface $x = X_1$ [Fig. 2(b)]. When the dendrite tips reach $x = X_1$ [Fig. 2(c)] liquid can still be fed across $x = X_b$. From this point on, however, macroporosity forms in the region $X_1 < x < X_{tip}$, where X_{tip} is the position of the dendrite tips. Solidification is completed when the rising eutectic front $x = X_{eut}$ meets the dropping liquid-air front $x = X_1$. In the current work the length of the domain, X_b , is chosen to coincide with this meeting point [Fig. 2(d)]. In this way, there will always be sufficient liquid in $x > X_b$ to feed the shrinkage in $0 < x \leq X_b$. Conceptually, the region in $x > X_b$ can be considered to play the role of a feeder (riser). Note

Fig. 2. Definition of the domain length X_b .

that with this boundary condition the mass in the solution domain, $0 < x < X_b$, will increase during the solidification process. On using representative phase densities ($\rho_l = 2438 \text{ kg m}^{-3}$ and $\rho_s = 2580 \text{ kg m}^{-3}$), a reasonable approximation, used in this work, for the domain length is $X_b = X_m(\rho_l/\rho_s)$.

A NUMERICAL SOLUTION APPROACH

Discretisation details

An explicit time integration of the governing equations [equations (3)–(5)] on a node-centered uniform grid of n control volumes [16] leads to the following set of discrete equations:

Heat transfer

$$[\rho H]_P = a_w T_w^o + a_E T_E^o - a_P T_P^o + S \quad (18)$$

where

$$a_w = [K]_w \frac{\Delta t}{(\Delta x)^2} \quad a_E = [K]_e \frac{\Delta t}{(\Delta x)^2} \quad a_P = a_w + a_E$$

$$S = [\rho H]_P^o + \frac{\Delta t}{\Delta x} (c_{P_l} (F_w^o T_P^o - F_e^o T_E^o) + (F_w^o - F_e^o) L)$$

Solute transfer

$$[\rho C] = [\rho C]_P^o + \frac{\Delta t}{\Delta x} (F_w^o C_{1_P}^o - F_e^o C_{1_E}^o) \quad (19)$$

Continuity

$$F_e = F_w + \frac{\Delta x}{\Delta t} ([\rho]_P^o - [\rho]_P) \quad (20)$$

where the convective terms have been 'upwinded' assuming that the flow is towards the chill face. In the above equations

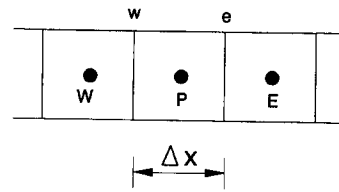


Fig. 3. Interior control volumes.

$$[K]_e = \left(\frac{[K]_P + [K]_E}{2} \right)$$

with a similar definition for $[K]_w$,

$$F = \rho_1 u$$

is the mass flow rate of liquid per unit area, the superscript o represents old values, the subscripts w and e represent the west and east faces of control volume P , and the subscripts W and E denote the nodes to the west and east of node P (see Fig. 3). Further, values for the nodal temperature T_{n+1} and nodal liquid concentration $(C_1)_{n+1}$ are evaluated via linear extrapolation.

Solution algorithm

(1) With the T , C_1 and F field values at the previous time step, the mixture enthalpy $[\rho H]$ and mixture solute density $[\rho C]$ are determined explicitly from equations (18) and (19).

(2) Then, using equations (1), (2), (7) and (8), the temperature T , the liquid fraction g_l and the liquid concentration C_1 , fields are 'extracted' from the calculated $[\rho H]$ and $[\rho C]$ fields (see Appendix 1).

(3) With the g_l field values from step 2, the density field ρ is evaluated via equation (6).

(4) Finally, using the current and previous values of the density field, the flow field to be used in the next time step is determined from equation (20).

An important component in the solver is the inclusion of a eutectic reaction [14]. Briefly, when the eutectic point is reached on the phase diagram ($T = T_{eut} = 821.2 \text{ K}$, $C_1 = 33.2\%$ for the aluminum-copper system), any remaining liquid isothermally transforms into two separate solid phases and partitioning of the solute between the liquid and solid phase does not take place. In the proposed solution, algorithm inclusion of the eutectic reaction is carried out in step 2; details are given in Appendix 1.

The objective of the model is calculation of the mixture concentration, i.e. $[C] = [\rho C]/[\rho]$, profile in the fully solidified casting (see Fig. 1). Grid independent values for $[C]$ are obtained with a mesh size of 100 nodes, and a time step of 0.9 times the explicit criteria limit; unless otherwise stated these will be the default sizes used in this study. The typical computational requirement, to full solidification, is 5 min on an IRIS Indigo R4000 workstation.

Table 1. Properties for the columnar dendritic Al-Cu alloy system

Property	Value	Unit
c_p	900	$J\ kg^{-1}\ K^{-1}$
c_p	1100	$J\ kg^{-1}\ K^{-1}$
$k_o^{[7]}$	0.172	—
K_l	100	$W\ m^{-1}\ K^{-1}$
K_s	200	$W\ m^{-1}\ K^{-1}$
L	3.95×10^5	$J\ kg^{-1}$
T_{eut}	821.2	K
T_i	933.2	K
C_{eut}	33.2	wt%
$\rho_1^{[13]}$	$2358.5 + 21.685C_1 + 7.2914 \times 10^{-2}C_1^2 - 7.2351 \times 10^{-4}C_1^3$	$kg\ m^{-3}$
$\rho_s^{[13]}$	$2564.7 + 1.4023C_1$	$kg\ m^{-3}$
$\rho_1^{out[13]}$	3232.3	$kg\ m^{-3}$
$\rho_s^{out[13]}$	3409	$kg\ m^{-3}$
C_0	4.1	wt%
h_{amb}^\dagger	$1684.21 - 4.3443t + 0.00449561t^2$ [where t is time (s)]	$W\ m^{-2}\ K^{-1}$
T_{amb}^\dagger	293	K
T_i	1020	K
X_b	0.1323	m

† Chosen to match experimental cooling conditions reported by Kato and Cahoon [11].

A TEST PROBLEM

As a test problem we will consider the aluminum-copper system modeled and experimentally investigated by Kato and Cahoon [11]. The key data to this problem are given in Table 1. Note that :

- (1) the choice of h_{amb} is made in order to closely match the predicted movements of the liquidus and solidus fronts with those of the experiments ;
- (2) the density variation with concentration, in both the solid and liquid phases, are obtained using the model proposed by Ganesan and Poirier [13].

VALIDATION

The proposed model (which will be referred to as the full model in the remainder of the text) and the associated solution approach is validated in three stages :

- (1) the heat transfer part of the model is validated on comparison with the semi-analytical heat balance integral solution proposed by Voller [17] ;
- (2) the solution for species transfer and the solute-temperature coupling are validated on comparison with the analytical solution of Flemings and Nereo [7] ;
- (3) finally, the one-dimensional model predictions are compared with the results from an independent two-dimensional fluid flow model [18], similar in nature to the model recently presented by Diao and Tsai [12].

Heat transfer

If the density is constant, e.g. $\rho = 2580\ kg\ m^{-3}$, then no inverse segregation occurs, and the governing equations model conduction-controlled solidification

of a binary alloy (e.g. see Clyne [19]). On assuming that the solidification occurs in the domain $0 \leq x \leq 0.2\ m$ and that the temperature at $x = 0$ is fixed at 573 K, predictions for the movement of the liquidus and eutectic fronts, obtained with the full model, can be compared with a semi-analytical heat balance integral solution [17]. The agreement between the model and semi-analytical predictions, shown in Fig. 4, is consistent with previous comparison studies [20] and hence confirms that the heat transfer elements in the full model are sound.

Solute transfer and solute temperature coupling

Following Flemings and Nereo [7], under the conditions of (i) constant densities in each phase, e.g. $\rho_s = 2580\ kg\ m^{-3}$ and $\rho_l = 2438\ kg\ m^{-3}$, (ii) prescribed linear liquidus (dendritic tips) and eutectic front movements, e.g.

$$\begin{aligned}
 X_{tip} &= \min \| 0.00041847t - 0.00298688, X_b \| \text{ (m)} \\
 X_{eut} &= 0.000269232t - 0.025 \text{ (m)} \tag{21}
 \end{aligned}$$

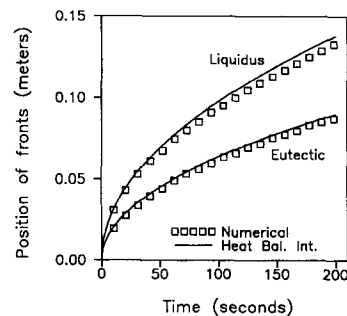


Fig. 4. Comparison between semi-analytical [17] and full model predictions of the liquidus and eutectic front movements.

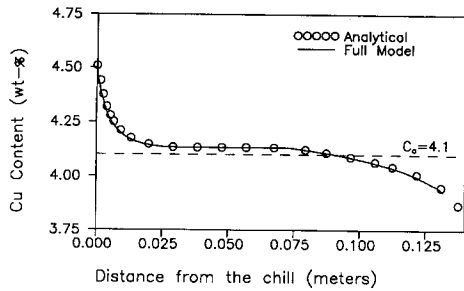


Fig. 5. Comparison between analytical [7] and full model predictions of the concentration profile.

and (iii) a linear liquid fraction between the eutectic and liquidus fronts (0–1), an analytical solution for calculating the mixture concentration at any specified point in the casting can be derived. Further, on calculating the liquid concentration and liquid fraction, this solution also allows for the calculation of the mixture enthalpy [ρH] at any specified point. In particular, the mixture enthalpy histories can be calculated at a set of n points corresponding to the control volumes used in the numerical solution of the full inverse segregation model. The validity of the treatment of the solute transport and solute temperature coupling in an implementation of the full model can then be checked on overwriting the mixture enthalpy values calculated with equation (18) with those obtained from the analytical model. When this is done, the model and analytical predictions for the mixture concentration profile are in very close agreement, (Fig. 5). From this result it can be concluded that the solute treatment (heat and solute transport and the temperature–solute coupling) used in the full model is appropriate.

Comparison with two-dimensional model results

Recently Swaminathan [18] has developed an independent two-dimensional fluid flow model of inverse segregation, which is similar in nature to the model reported by Diao and Tsai [12]. Figure 6 compares

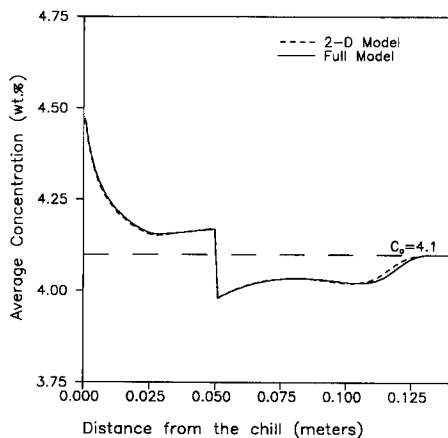


Fig. 6. Comparison between two-dimensional model and full model predictions of the concentration profile when the dendrite tips reach X_b .

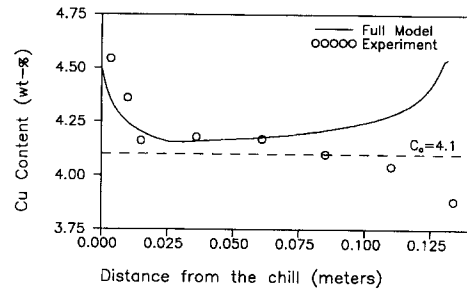


Fig. 7. Full model predictions of the concentration profile compared with experimental measurements [11].

predictions (inverse segregation profile at the point when the dendritic tips just reach $x = X_b$) obtained with the proposed model and the two-dimensional model [18]. The predictions are in close agreement, which indicates that: (i) the one-dimensional assumption used in developing the model is sound, and (ii) the solution method adopted is appropriate.

INITIAL APPLICATION TO THE TEST PROBLEM

Figure 7 shows predictions of the mixture concentration obtained with the direct use of the full model using the data given in Table 1. These results predict the inverse segregation at the chill face, but deviate dramatically from the experimental results in the later regions of solidification; notably there is a large 'turn up' (positive segregation) in the concentration profile not seen in the experiments or the limiting analytical solution. Changing the model parameters, in particular cooling rate, density and domain length X_b , has very little effect on the shape of the predicted concentration profile; i.e. the solute turn up at the end persists. This result is somewhat puzzling, especially when one considers that the solute transport equation is essentially identical to the initial equations used in deriving the analytical inverse segregation model [7]. Furthermore, in the limiting case of prescribed linear front movements and a linear liquid fraction profile, the results from the full model are in close agreement with the analytical solution and experiments (Fig. 5). This leads us to believe that, despite the excellent agreement with experimental measurements, the assumption of a linear liquid fraction that 'lies at the heart' of the analytical model may be invalid. Supporting evidence for this view point comes from two sources. In the first place, the full model, based on the transport equations (3)–(5), predicts liquid fractions which are far from linear (Fig. 8) but consistent with liquid fraction profiles presented elsewhere in the literature [19]. In the second place, consider the predicted temperature profiles in the mushy region. Figure 8 compares the temperature profiles predicted by the full model and the analytical model, close to the half-way point in the solidification. From a practical point of view, the temperature profile predicted by the analytical model is not realizable in

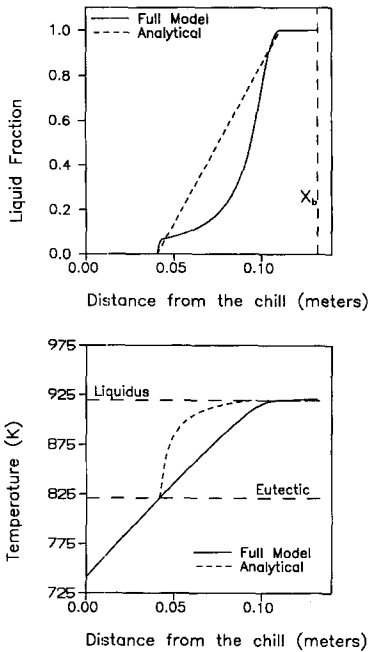


Fig. 8. Comparison of analytical and full model predictions for (a) the liquid fraction distribution, and (b) the temperature profile.

that it requires a very large discontinuity in the gradient to be present at the eutectic front.

THE ROLE OF MICROPOROSITY

The results presented in Fig. 7 lead us to the conclusion that important physics has been omitted from the initial derivation of the full model. A possible candidate in this respect is the effect of microporosity. Briefly, in aluminum-copper alloys, microporosity forms at low liquid fractions due to the combined effect of the ‘choking’ of the flow as the dendritic spaces narrow and the precipitation of hydrogen [21–25]. The nature of porosity can be better understood on noting the following ‘rules of thumb’ obtained from the literature [11, 21–31]:

- (1) in a well-degassed casting, microporosity does not form in the vicinity of the chill face [24];
- (2) the range of microporosity values (vol%) observed in aluminum alloys ranges between 0.1 and 5% [23, 26, 27];
- (3) the microporosity increases as a function of distance from the chill [11, 26, 30];
- (4) the metallostatic head (the height of liquid metal in the feeder) affects the microporosity [23, 25, 31].

The effect of microporosity on inverse segregation is to reduce the shrinkage feeding and thereby reduce the mass flow rate of solute towards the chill. In an ad hoc treatment involving the specification of a friction factor which restricts flowback, Kato and Cahoon [11] investigated the effects of microporosity on inverse

segregation in equiaxed systems. Using an analytical model with the now suspect assumption of a linear liquid fraction, these authors showed that accounting for the microporosity in equiaxed systems does have a beneficial effect (when comparing with experiments). These authors claim, however, that the levels of microporosity that occur in columnar dendritic systems (such as aluminum-copper alloys) are too small to have an effect. In the light of the non-physical features predicted by our inverse segregation model, we would like to re-investigate this point.

Modeling microporosity formation in metal casting is a current and active field of research [23–31]. State-of-the-art models involve a detailed accounting of the coupling of the thermodynamics and fluid flow at the local scale of the mushy region. In addition, the majority of papers are directed at ‘plate casting’ geometries and many involve alloys other than aluminum-copper. As such we feel that the inclusion of a microporosity model in the proposed inverse segregation model is beyond the scope of the current paper and, in order to account for the effects of microporosity, we propose to follow the friction factor approach previously used by Kato and Cahoon [11] and by Murakami *et al.* [26]. In this approach, before the numerically calculated flow field values are used in the next time step, it is multiplied by a friction factor, $ff(x, t) < 1$, i.e. at node P

$$F_c^* = ff F_c \tag{22}$$

where the superscript * denotes the modified value. Further, using continuity, the nodal microporosity field formed at each time step can be calculated as

$$g_{por} = g_{por}^o + \left[\frac{(F_c^* - F_w^*)\Delta t + (\rho_p - \rho_l)\Delta x}{\rho_l \Delta x} \right] \tag{23}$$

This microporosity distribution is easily incorporated into the inverse segregation model. The main modification is that the solid volume fraction g_s in equations (6)–(8) is redefined as $g_s = (1 - g_l - g_{por})$. In the current work the choice of the friction factor is

$$ff(x_p, t) = 1 - (1 - Y)(1 - g_{1p})^2$$

where

$$Y = 1 - 0.8 \left[\frac{\exp\left(\frac{4x_p}{X_b}\right) - 1}{\exp(4) - 1} \right]$$

and x_p is the node position. This can be considered to be a somewhat arbitrary choice; note, however, that the resulting microporosity distribution, on complete solidification (Fig. 9), is

- (1) consistent with the microporosity rules of thumb presented above, and
- (2) similar in form and magnitude to the microporosity distribution measured and predicted by

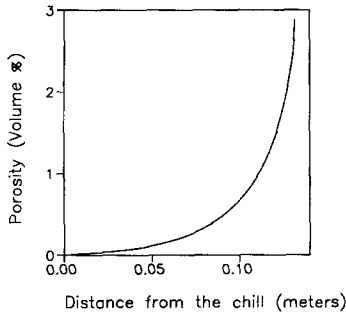


Fig. 9. Predicted microporosity distribution.

Zou and Doherty [32] in unidirectional castings of aluminum alloys.

Further, use of this factor in the full model leads to the prediction of a concentration profile in close agreement with the experiment (Fig. 10). Hence, the inclusion of microporosity into the full model does have an effect on the qualitative behavior of the model predictions. This indicates that microporosity should be included in inverse segregation models of columnar dendritic systems.

LOCAL BEHAVIOR

The current inverse segregation model uses a Scheil treatment that assumes, at the local scale of the REV, complete liquid mass diffusion and zero solid mass diffusion. Results using the Scheil approach will be different from those based on the more commonly used equilibrium lever rule, which assumes complete diffusion at the local scale, in both the solid and the liquid [1, 2, 4, 12]. The principal reason for this is that, no matter what the initial solute concentration, a Scheil-based model will always predict a eutectic fraction, whereas at an initial solute concentrations below the solid eutectic concentration (5.65 wt% in the aluminum-copper system) a lever-based model will not. Since the eutectic reaction represents the major density change in the mushy region ($\rho_i^{\text{eut}} = 3232 \text{ kg m}^{-3}$, $\rho_s^{\text{eut}} = 3409 \text{ kg m}^{-3}$), there should be a significant difference between Scheil- and lever-based models. This is confirmed on reference to the dashed line in Fig. 10, which shows the concentration profile predicted by the full model using a

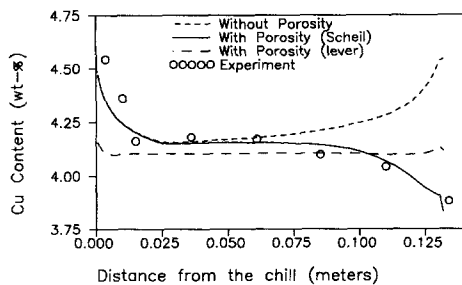


Fig. 10. Predictions of concentration profiles when microporosity is included.

lever assumption. It is clear that the presence of local-scale diffusion has a significant effect on inverse segregation.

CONCLUSIONS AND DISCUSSION

Our original intention in studying inverse segregation models was to develop a test bed where we could develop a micro-macro model that could account for non-equilibrium effects (in particular solid solute diffusion in the mushy zone). We felt that the experimentally validated one-dimensional analytical models [6, 7] reported in the literature were more than adequate for describing the essential features of inverse segregation. Our rationale for developing a numerical model based on the governing transport equations was motivated by the need to provide a framework into which the micro-model describing the local-scale diffusion of solute [33, 34] could easily be fitted. Problems arose in this approach, however, when it was found that the predictions from the model based on the governing transport equations did not match the available experimental results or the analytical solution. This was a point that we felt deserved careful study in order to resolve or at least explain the reasons for the discrepancy. The major findings from this study are:

- (1) in two limiting cases, results obtained from a numerical model, based on the governing transport equations (3)–(5), agree with the available analytical solutions;
- (2) the validity of the underlying assumption of a linear liquid fraction profile used in analytical inverse segregation models has been called into question;
- (3) the qualitative nature of the full model predictions can be dramatically improved on introducing a microporosity treatment; small realistic amounts of microporosity have a large effect on the nature of the full model predictions;
- (4) extreme treatments of the local-scale mass diffusion (i.e. microsegregation) have a marked effect on the inverse segregation results.

The last two points indicate that a complete model of inverse segregation will require appropriate treatments of (i) the microporosity formation, and (ii) the local-scale mass diffusion. Investigation of these points will be the objective of future studies.

Acknowledgement—The authors would like to acknowledge the Minnesota Supercomputer Institute for furnishing a computer resources grant.

REFERENCES

1. W. D. Bennon and F. P. Incropera, The evolution of macro-segregation in statically cast binary ingots, *Metall. Trans.* **18B**, 611–616 (1987).
2. C. Beckermann and R. Viskanta, Double-diffusive convection during dendritic solidification of a binary mixture, *PhysicoChem. Hydrodyn.* **10**, 195–213 (1988).
3. V. R. Voller, A. D. Brent and C. Prakash, The modelling

- of heat, mass and solute transport in solidification systems, *Int. J. Heat Mass Transfer* **32**, 1719–1731 (1989).
4. G. Amberg, Computation of macrosegregation in an iron-carbon cast, *Int. J. Heat Mass Transfer* **34**, 217–227 (1991).
 5. M. C. Flemings, *Solidification Processing*. McGraw-Hill, New York (1974).
 6. J. S. Kirkaldy and W. V. Youdelis, Contribution to the theory of inverse segregation, *Trans. Metall. Soc. AIME* **212**, 833–840 (1958).
 7. M. C. Flemings and G. E. Nereo, Macro-segregation. Part I, *Trans. Metall. Soc. AIME* **239**, 1449–1461 (1967).
 8. M. C. Flemings, R. Mehrabian and G. E. Nereo, Macro-segregation. Part II, *Trans. Metall. Soc. AIME* **242**, 41–49 (1968).
 9. M. C. Flemings and G. E. Nereo, Macro-segregation. Part III, *Trans. Metall. Soc. AIME* **239**, 50–55 (1968).
 10. W. V. Youdelis, Theory of inverse segregation, *Proceedings of the Conference on the Solidification of Metals*. Iron and Steel Institute, London (1969).
 11. H. Kato and J. R. Cahoon, Inverse segregation in directionally solidified Al-Cu-Ti alloys with equiaxed grains, *Metall. Trans.* **16A**, 579–587 (1985).
 12. Q. Z. Diao and H. L. Tsai, Modeling of solute redistribution in the mushy zone during solidification of aluminum-copper alloys, *Metall. Trans.* **24A**, 963–973 (1993).
 13. S. Ganesan and D. R. Poirier, Densities of aluminum-rich aluminum-copper alloys during solidification, *Metall. Trans.* **18A**, 721–723 (1987).
 14. S. H. Avner, *Introduction to Physical Metallurgy* (2nd Edn). McGraw-Hill, Singapore (1987).
 15. J. Ni and C. Beckermann, A volume averaged two-phase model for transport phenomena during solidification, *Metall. Trans.* **22B**, 349–361 (1991).
 16. S. V. Patankar, *Numerical Heat Transfer and Fluid Flow*. Hemisphere, Washington, DC (1980).
 17. V. R. Voller, Development and application of a heat balance integral method for analysis of metallurgical solidification, *Appl. Math. Model.* **13**, 3–11 (1989).
 18. C. R. Swaminathan, Numerical modeling of filling and solidification in metal casting processes, Ph.D. Thesis, University of Minnesota (1994).
 19. T. W. Clyne, Numerical modelling of directional solidification of metallic alloys, *Metal Sci.* **16**, 441–450 (1982).
 20. V. R. Voller and C. R. Swaminathan, General source-based method for solidification phase change, *Numer. Heat Transfer B* **19**, 175–189 (1991).
 21. T. S. Pivonka and M. C. Flemings, Pore formation during solidification, *Trans. Metall. Soc. AIME* **236**, 1157–1165 (1966).
 22. D. E. Talbot, Effects of hydrogen in aluminum, magnesium, copper and their alloys, *Int. Metall. Rev.* **20**, 166–184 (1975).
 23. K. Kubo and R. D. Pehlke, Mathematical modeling of porosity formation in solidification, *Metall. Trans.* **16B**, 359–366, (1985).
 24. D. R. Poirier, K. Yeum and A. L. Maples, A thermodynamic prediction for microporosity formation in aluminum-rich Al-Cu alloys, *Metall. Trans.* **18A**, 1979–1987, (1987).
 25. J. Campbell, *Castings*. Butterworth-Heinemann, Oxford (1991).
 26. K. Murakami, C. Y. Liu and T. Okamoto, Feeding to casting where a riser is in a pasty state. In *Solidification Processing*, pp. 287–290. The Institute of Metals, London (1987).
 27. Y. W. Lee, E. Chang and C. F. Chieu, Modeling of feeding behaviour of solidifying Al-7Si-0.3Mg alloy plate casting, *Metall. Trans.* **21B**, 715–722 (1990).
 28. J. D. Zhu and I. Ohnaka, Computer simulation of interdendritic porosity in aluminum alloy ingots and casting. In *Modeling of Casting, Welding and Advanced Solidification Processes V* (Edited by M. Rappaz, M. R. Ozgu and K. W. Mahin), pp. 435–442. TMS, Warrendale, PA (1990).
 29. J. Ampuero, A. F. A. Hoadley and M. Rappaz, Numerical and experimental study of microporosity evolution during the solidification of metallic alloys. In *Modeling of Casting, Welding and Advanced Solidification Processes V* (Edited by M. Rappaz, M. R. Ozgu and K. W. Mahin), pp. 449–454. TMS, Warrendale, PA (1990).
 30. H. D. Brody, S. Viswanathan and R. A. Stoehr, Predicting shrinkage microporosity in aluminum-copper alloys. In *Modeling of Casting, Welding and Advanced Solidification Processes V* (Edited by M. Rappaz, M. R. Ozgu and K. W. Mahin), pp. 455–460. TMS, Warrendale, PA (1990).
 31. H. Huang, V. K. Suri, N. El-Kaddah and J. T. Berry, The effect of interdendritic feeding on microporosity formation. In *Modeling of Casting, Welding and Advanced Solidification Processes V* (Edited by T. S. Pivonka, V. R. Voller and L. Katgerman), pp. 219–460. TMS, Warrendale, PA (1993).
 32. J. Zou and R. Doherty, Private communication (October 1993).
 33. V. R. Voller and S. Sundarraj, Modeling of micro-segregation, *Mater. Sci. Technol.* **9**, 474–481 (1993).
 34. S. Sundarraj and V. R. Voller, The binary alloy problem in an expanding domain: the microsegregation problem, *Int. J. Heat Mass Transfer* **36**, 713–723 (1993).

APPENDIX 1

Calculation of T , C_1 and g_1 fields

Assuming constant phase densities, equations (1), (2), (7) and (8) can be combined into two non-linear equations in T and g_1 :

$$[\rho H] = a_1 g_1 + a_2 T + a_3 g_1 T \quad (\text{A1})$$

where

$$a_1 = \rho_1 L \quad a_2 = \rho_s c_p (1 - g_{\text{por}}) \quad a_3 = \rho_1 c_p - \rho_s c_p \quad (\text{A2})$$

and

$$[\rho C] = b_1 + b_2 g_1 + b_3 T + b_4 g_1 T \quad (\text{A3})$$

where

$$b_1 = \int_0^{g_0^*} \rho_s C_s \, d\alpha + \left(\frac{\rho_s^* k_0 T_f}{m_1} \right) (g_{\text{por}}^0 - g_{\text{por}} + g_1^0)$$

$$b_2 = \left(\frac{\rho_1 - \rho_s^* k_0}{m_1} \right) T_f$$

$$b_3 = - \left(\frac{\rho_s^* k_0}{m_1} \right) (g_{\text{por}}^0 - g_{\text{por}} + g_1^0)$$

$$b_4 = - \left(\frac{\rho_1 - \rho_s^* k_0}{m_1} \right). \quad (\text{A4})$$

For a given prescription of the microporosity, equations (A1) and (A3) can be solved using Newton's method, and C_1 obtained using equation (1). Important points to note are:

(1) When a lever assumption is used, the T , C_1 and g_1 are extracted from equations (12) and (13). In this case, the resulting non-linear equations will have the same form as equations (A1) and (A3) with the coefficients of equation (A3) given by

$$\begin{aligned}
 b_1 &= \left(\frac{\rho_s k_0 T_f}{m_1} \right) (1 - g_{\text{por}}) \\
 b_2 &= \left(\frac{\rho_1 - \rho_s k_0}{m_1} \right) T_f \\
 b_3 &= - \left(\frac{\rho_s k_0}{m_1} \right) (1 - g_{\text{por}}) \\
 b_4 &= - \left(\frac{\rho_1 - \rho_s k_0}{m_1} \right). \quad (\text{A5})
 \end{aligned}$$

(2) In cases where no microporosity forms, g_{por} is set to zero.

(3) A non-constant phase density can be treated by successive substitution in the Newton's solver.

(4) On convergence, the T , g_1 and C_1 fields are subjected to the following conditions to reset their values to the correct value if they lie outside the phase change range or the eutectic reaction is occurring:

(i) if $(T > T_{\text{liq}})$ then

Reset: $C_1 = C_o$ $g_1 = 1$ $\rho_1 = \rho_l$ and

$$T = \left[\frac{[\rho H] - \rho_1 L}{\rho_1 c_{p_1}} \right] \quad (\text{A6})$$

(ii) if $(C_1 > C_{\text{eut}})$ then

Reset: $C_1 = C_{\text{eut}}$ $T = T_{\text{eut}} = 0$ $\rho_s = \rho_s^{\text{eut}}$ $\rho_1 = \rho_1^{\text{eut}}$

and

$$g_1 = \left(\frac{[\rho H]}{\rho_1 L} \right) \quad (\text{A7})$$

(iii) If $(g_1 \leq 0)$ then

Reset: $C_1 = C_1^{\text{old}}$ $g_1 = 0$ $\rho_s = \rho_s^{\text{old}}$

$$T = \left(\frac{[\rho H]}{\rho_s c_{p_s}} \right). \quad (\text{A8})$$

Note that steps (i), (ii) and (iii) are performed in the order shown and that step (ii) accounts for the eutectic formation.